

Combination of multi-scale and multi-edge X-ray spectroscopy for investigating the products obtained from the interaction between kaolinite and metallic iron in anoxic conditions at 90 °C

Camille Rivard · Emmanuelle Montargès-Pelletier · Delphine Vantelon ·
Manuel Pelletier · Chithra Karunakaran · Laurent J. Michot · Frédéric Villieras ·
Nicolas Michau

Received: 13 March 2012 / Accepted: 3 November 2012 / Published online: 16 December 2012
© Springer-Verlag Berlin Heidelberg 2012

Abstract In the context of radioactive waste repository in geological formation, kaolinite-metallic iron interaction in chlorine solution was conducted in batch experiments, under anoxic conditions at 90 °C during 9 months. After a mineralogical characterization at a global scale, products were analyzed at the micrometer and nanometer scales by X-ray absorption spectroscopic techniques (XAS and STXM). Absorption at Al, Si and Fe edges was

investigated to have a complete overview of the distribution and status of constituting elements. Whereas Si K-edge results do not evidence significant evolution of silicon status, investigations at Al K-edge and Fe L-edges demonstrate variations at aggregate and particle scales of $^{IV}Al:^{VI}Al$ and $Fe^{2+}:Fe^{3+}$ ratios. Spectroscopic data evidence the systematic crystallization of Fe-serpentine onto the remaining particles of kaolinite and the absence of pure species (kaolinite or Fe-serpentine). Combination of spatially resolved spectroscopic analyses and TEM-EDXS elemental distribution aims to calculate unit cell formulae of Fe-serpentine layers and abundance of each species in mixed particles. For most of the investigated particles, results reveal that the variations of particles composition are directly linked to the relative contributions of kaolinite and Fe-berthierine in mixed particles. However, for some particles, microscale investigations evidence crystallization of two other Fe-serpentine species, devoid of aluminum, cronstedtite and greenalite.

Electronic supplementary material The online version of this article (doi:10.1007/s00269-012-0552-6) contains supplementary material, which is available to authorized users.

C. Rivard · E. Montargès-Pelletier · M. Pelletier ·
L. J. Michot · F. Villieras
Laboratoire Environnement et Minéralurgie, CNRS, UMR 7569,
54500 Vandœuvre-lès-Nancy, France
e-mail: emmanuelle.montarges@univ.lorraine.fr

C. Rivard · E. Montargès-Pelletier · M. Pelletier ·
L. J. Michot · F. Villieras
Laboratoire Environnement et Minéralurgie, Université de
Lorraine, UMR 7569, 54500 Vandœuvre-lès-Nancy, France

Present Address:

C. Rivard (✉)
European Synchrotron Radiation Facility,
38000 Grenoble, France
e-mail: camille.rivard@esrf.fr; rivard.camille@gmail.com

D. Vantelon
Synchrotron Soleil, St Aubin, 91192 Gif-sur-Yvette, France

C. Karunakaran
Canadian Light Source, University of Saskatchewan, Saskatoon,
SK S7N 0X4, Canada

N. Michau
Agence nationale pour la gestion des déchets radioactifs,
ANDRA, 92298 Châtenay-Malabry, France

Keywords X-ray absorption spectroscopy · XAS ·
STXM · Phyllosilicate · Berthierine · Iron

Introduction

In the context of the geological disposal of high-level radioactive waste (HLW), ANDRA (French national radioactive waste management agency) selected the Callovo-Oxfordian rock (COx) from the ZIRA (Interest Zone for in-depth study, Bure, France) as a candidate host rock. This rock contains around 40 % of clay minerals: illite, interstratified illite-smectite, chlorite and kaolinite, the remaining portion being mainly quartz, carbonates and feldspars. For the future functioning of the disposal site, it

is of prime importance to understand the interactions between the water-saturated clay formation and steel containers, through an in-depth analysis of iron–clay interactions. Previous studies have investigated the mineralogical transformations resulting from the contact of COx rock with iron either in batch experiments using metallic iron powder under anoxic atmosphere (de Combarieu et al. 2007) or by placing iron bars directly in contact with heated COx rock (Schlegel et al. 2008). Such approaches provide valuable information; however, the complexity of the COx composition prevents from deciphering the role of each individual rock component. For this reason, it is relevant to analyze the reactions between pure clay phases and metallic iron in conditions close to those of underground repository, that is, moderate temperatures close to 80 °C and in anoxic conditions. Concerning kaolinite mineral, experiments carried out at 80 °C in isolated reactors (Kohler 2001; Perronnet 2004) evidenced the formation of Fe-rich serpentine-like species upon contact between metallic iron and kaolinite/smectite mixture or pure kaolinite.

We performed a detailed study of interaction between pure KGa-2 kaolinite and powdered iron at 90 °C in anoxic conditions for reaction times ranging between 1 and 9 months (Rivard et al. 2013). The resulting solutions and solids were then studied by chemical analysis, X-ray diffraction, infrared and Mössbauer spectroscopies, electron microscopy and high-resolution argon adsorption. We then evidenced (1) a fast but partial oxidation of metallic iron, (2) the formation of low amount of magnetite (3 %), (3) a destabilization of the initial clay material, (4) an iron enrichment in the modified clay particles and (5) the formation of a 7 Å iron-bearing clay mineral, identified as berthierine (Fe-serpentine family). All the results could be interpreted by assuming that berthierine layers were formed from the dissolution of kaolinite edge faces with a subsequent precipitation of iron-rich clay layers onto basal surfaces of remaining kaolinite. Still, some fine details of this scenario remain misunderstood. Indeed, local chemical analyses obtained by TEM-EDXS (transmission electron microscopy combined with energy dispersive X-rays spectroscopy) reveal significant variations in iron content for different particles. This could be due to variations in kaolinite:berthierine ratios between particles, but could also result from changes in the composition of the newly formed berthierine from one particle to another. Analyzing these possible changes requires carrying out local-scale spectroscopic analyses of aluminum, silicon and iron status that would also allow determining more precisely the layer composition of the newly formed Fe-serpentine.

The present paper is then devoted to a detailed X-ray absorption spectroscopy investigation of the reaction products obtained after 9 months between pure KGa-2 kaolinite

and powdered metallic iron at 90 °C under anoxic conditions. Different spatial scales were explored by combining the use of various synchrotron-based techniques. First of all, bulk X-ray absorption spectroscopy data allow obtaining average information that is directly comparable to that derived from previously obtained XPS or Mössbauer analyses (Rivard et al. 2013). Using micrometer size X-ray beams, it was then possible to obtain X-ray absorption data at the Al, Si and Fe K-edges at the spatial scale of particle aggregates. Finally, as the individual particles are micrometer or sub-micrometer in size, STXM (scanning transmission X-ray microscopy) experiments were carried out at the Fe L_{2,3}-edges, Si and Al K-edges, with a spatial resolution down to 30 nm. Here, we have demonstrated that such a combination of techniques is crucial for refining reaction mechanisms and obtaining a better description of the mineralogy of the newly formed clay phases.

Materials and methods

Metallic iron–kaolinite interaction

Georgia kaolinite (KGa-2) was provided by the Clay Mineral Society. Its unit cell formula is $(\text{Si}_{1.92}\text{Al}_{0.08})(\text{Al}_{1.9}\text{Ti}_{0.07}\text{Fe}_{0.03}^{3+})\text{Ca}_{0.002}\text{Na}_{0.005}\text{K}_{0.001}\text{O}_5(\text{OH})_4$ (Mermut and Cano 2001). Kaolinite is a layered silicate mineral with a 1:1 structure (each layer is made by the superimposition of one tetrahedral sheet and one octahedral sheet). Powdered metallic iron, provided by Aldrich[®], presents a purity >99.5 % and a mean diameter of 40 μm. The composition of the chlorine solution used in the experiments ($\text{NaCl} = 0.0207 \text{ mol kg}^{-1}$, $\text{CaCl}_2 = 0.0038 \text{ mol kg}^{-1}$) is close to that of interstitial water in the COx geological formation.

Kaolinite (6 g), metallic iron (2 g) and solution (120 mL) were introduced in Parr[®] autoclaves and kept at 90 °C under anoxic atmosphere during 9 months. After reaction, solid and liquid phases were separated by centrifugation (46,000 g during 45 mn). Solid fraction was freeze-dried, powdered and kept under anoxic atmosphere. Initial materials and reaction conditions are described in more details in Rivard et al. (2013). For a proper analysis of X-ray absorption spectroscopy data, various pure minerals were used as references. Their list and average formulae are reported in Table 1.

XAS measurements

Sample preparation

As SEM observations revealed that the concentration in morphologically transformed phases was maximal around

Table 1 Reference products (clays, iron oxides and oxyhydroxides) studied by XAS and/or STXM

Mineral	Reference	Family	Formulae	x_t	XAS	STXM
Berthierine BStA	Moëlo et al. (2009)*	Serpentine	$(\text{Si}_{1.3}\text{Al}_{0.7})(\text{Fe}_{2.13}^{2+}\text{Al}_{0.7}^{3+}\text{V}_{0.03}^{2+}\text{Mg}_{0.14}^{2+})\text{O}_3(\text{OH})_4$	0.35	x	x
Chamosite	Aja and Darby Dyar (2002)	Chlorite	$(\text{Si}_3\text{Al})(\text{Al}_{2.98}\text{Mn}_{0.05}\text{Ca}_{0.03}\text{Zn}_{0.01}\text{Fe}_{5.43}^{2+}\text{Fe}_{0.60}^{3+}\text{Mg}_{2.3})\text{O}_{12}(\text{OH})_6$	0.25	x	
Magnetite	Prolabo	Iron oxide	Fe_3O_4		x	x
Maghemite	Alfa Aesar	Iron oxide	$\gamma\text{-Fe}_2\text{O}_3$			x
Goethite	BASF	Iron oxyhydroxide	$\text{FeO}(\text{OH})$			x
Illite	Bardot et al. (1998)	Illite du Puy	$(\text{Si}_{3.55}\text{Al}_{0.45})(\text{Al}_{1.27}\text{Fe}_{0.36}^{3+}\text{Mg}_{\text{tri}0.21}\text{Mg}_{\text{di}0.23})\text{Ca}_{0.01}\text{Na}_{0.13}\text{K}_{0.53}\text{O}_{10}(\text{OH})_2$	0.1125	x	
Montmorillonite SWy-2	Clay Mineral Society	Montmorillonite	$(\text{Si}_{3.87}\text{Al}_{0.13})(\text{Al}_{1.53}\text{Fe}_{0.21}^{3+}\text{Mg}_{0.24}\text{Fe}_{0.02}^{2+})\text{Na}_{0.39}\text{O}_{10}(\text{OH})_2$	0.035	x	
Nontronite NAU- 2	Clay Mineral Society	Nontronite	$(\text{Si}_{3.78}\text{Al}_{0.08}\text{Fe}_{0.14}^{3+})(\text{Fe}_{1.77}^{3+}\text{Al}_{0.17}\text{Mg}_{0.03})\text{Na}_{0.36}\text{O}_{10}(\text{OH})_2$	0.055	x	
Saponite	Synthetic saponite	Saponite	$(\text{Si}_{3.3}\text{Al}_{0.7})\text{Mg}_3\text{Na}_{0.7}\text{O}_{10}(\text{OH})_2$	0.175	x	

Tetrahedral substitution rate x_t is equal to the total number of atoms occupying tetrahedral sites versus the total number of tetrahedral sites. *Moëlo et al. (2009) refer to an oral presentation at French Clay Group meeting

remaining metallic iron grains (Rivard et al. 2013), we carried out a preliminary separation of fine and coarse fractions by successive re-suspension and sedimentation in ethanol, using ultrasound to enhance particle dispersion. These operations were repeated until the supernatant was particle free. The settled material refers to the coarse fraction (C), and the centrifugation of the supernatant at 45,000 g provides the fine fraction (F). Both fractions were subsequently dried under nitrogen atmosphere. The coarse fraction contains nodules of transformed clay particles as well as large (around 30 μm) and well-crystallized magnetite particles. Residual metallic iron grains were found in the center of these clay nodules. In contrast, the fine fraction appears to be mainly constituted by clay particles (Rivard et al. 2013).

For micro-XAS investigations, fractions were resin-embedded in order to prepare self-supported slices. Resin was prepared from Kit Embed 812 (Euromedex), and impregnation was carried out by three successive acetone–resin exchanges. Resulting samples were heated at 60 °C during 24 h for polymerization. Slices of 50–100 μm were cut and preliminarily screened with optical and electron microscopes to check for particle distribution and pre-select interesting zones.

For bulk-XAS analyses, samples were mixed with cellulose and pressed into pellets. The initial kaolinite was also prepared as oriented films for oriented spectra measurements. Powder of kaolinite was dispersed into deionized water for 24 h. Then, five drops of the suspension were deposited on a copper plate and air dried. The process was repeated five times in order to obtain a deposit with sufficient thickness.

Data collection

XAS and XRF experiments were carried out at the LUCIA beamline (Synchrotron SOLEIL, St Aubin, France) that is dedicated to X-ray absorption and fluorescence in the tender X-ray domain (Flank et al. 2006). Si (111) and KTP (011) crystals were used for experiments at the iron K-edge (7,000–8,000 eV) and at aluminum and silicon K-edges (1,500–2,000 eV), respectively. Monochromator calibration was performed by using iron and aluminum foils and setting the first inflexion points at 7,112 and 1,559 eV, respectively. Beam focusing on the sample was achieved using mirrors in Kirkpatrick-Baez configuration. A beam size of 3 μm (H) \times 3 μm (V) (full width at half maximum—FWHM) was thus obtained at high energy (Fe K-edge), whereas a 3 μm (H) \times 7 μm (V) (FWHM) was obtained at lower energy. Sample positioning was ensured by using a micrometric x, y, z stage. Data were collected at room temperature and under vacuum, in fluorescence yield mode using a Silicon Drift Diode mono-element fluorescence detector. The different fluorescence lines were discriminated using a multi-channel analyzer and their intensity directly obtained from the area of the XRF spectra. The X-ray experiments used a dwell time of 1 s.

Investigated zones were selected within wide fluorescence maps at 8,000 eV (500–1,000 μm^2 area with 50 μm step), to acquire small fluorescence maps below and above the iron edge (7,000 and 8,000 eV) with 1–5 μm step. Points of Interest (POI's) were then selected for X-ray absorption spectra in XANES and EXAFS energy ranges, with energy steps of 0.2 and 2 eV, respectively. Typical

acquisitions were performed by counting 4 s per point and cumulating four spectra. POIs will be referred to as C-pi for the coarse fraction, and F-pi for the fine fraction ($i = 1$ to n). After switching to low energy crystals, in order to perform XAS analyses at Al and Si K-edges, maps with 1–5 μm steps were collected to recover POIs investigated at Fe edge. XANES spectra were then collected in fluorescence yield mode using 0.1 and 0.2 eV energy step in the edge region for Al and Si, respectively.

Bulk XAS measurements at Fe K-edge (*F* fraction only) were performed on the SAMBA beamline at SOLEIL, France (Belin et al. 2005). Calibration of the Si (220) monochromator was performed using a Fe foil setting the first inflexion point at 7,112 eV. Experiments were performed under secondary vacuum, at room temperature and in transmission mode.

Data reduction and analysis

XANES and EXAFS data were reduced using standard normalization procedures using the ATHENA package (Newville 2001; Ravel and Newville 2005). E_0 edge energy was chosen in the higher part of the edge step, as the maximum of the first derivative. Spectra were normalized relative to the absorption above the threshold, and the background was linearly fitted using the Autobk algorithm (Newville et al. 1993). For EXAFS spectra collected at the Fe K-edge, data were transformed from energy space E (eV) to wave vector space k (\AA^{-1}) by removing a smooth post-edge background function approximating absorption by an isolated atom. The resulting $\chi(k)$ function was weighted by k^3 to avoid oscillations damping at high k values.

Theoretical EXAFS spectra could be calculated following the crystallographic reduced data from cronstedtite (WWW-MINCRYST 2012, CRONSTEDTITE-1077). The atomic coordinates were modified to take into account the fact that in berthierine, tetrahedra are occupied by silicon only. Furthermore, to be able to reproduce backscattering paths of $^{\text{VI}}\text{Al}$, one octahedral site was filled with Al instead of Fe. The paths list was then obtained by running programs ATOMS and FEFF6 (included in the ARTEMIS subroutine (Newville 2001; Ravel and Newville 2005)). Individual scattering paths were selected for fitting on the basis of the number of implied scattering legs, of their relevance and relative contribution to the EXAFS signal (calculated by FEFF). From what is known about the 7 \AA clay structure and also from our previous experience on Fe-bearing phyllosilicates (Vantelon et al. 2003), the second shell can be described as a first approximation, as a sum of two sheets, (1) edge-sharing neighbors of the octahedral sheet and (2) corner-sharing neighbors of the tetrahedral sheet. For the latter, the number of neighbors was fixed to

two as the newly formed Fe-bearing phase was shown to be a 1:1 clay phase. For the octahedral sheet, its occupancy is directly linked to the valence of cations. Indeed, for a dioctahedral sheet in which occupancy is equal to 2:3, trivalent cations should be predominant, and the number of edge-sharing neighbors should be fixed to 3. For a trioctahedral sheet, in which occupancy is equal to 3:3, divalent cations (Fe^{2+} in our precise case) should predominate and the number of edge-sharing neighbors should be fixed to six. In the fitting strategy, we explored various possibilities in terms of octahedral sheet occupancy going from one extreme assumption: 3 Al, to another extreme one: 6 Fe^{2+} . The fitting analysis was restrained to the first two peaks of the radial distribution function obtained by a Fourier transform of EXAFS oscillations, and only simple scattering paths ($n = 2$) were considered for fitting. The amplitude factor (S_0^2), taking into account the multi-excitations effect (shake-up and shake-off processes) (Teo 1986), was fixed in order to decrease the number of fitting parameters, and on the basis of theoretical values, it was set at 0.7 for all shells.

STXM measurements

Sample preparation

One drop (10 microliters) of fine fraction alcoholic suspension was placed on a carbon-coated copper grid and evaporated. The grid was fixed on the sample holder and pre-screened using an optical microscope to locate particles, check the quality of the dispersion and pre-select interesting zones. The sample holder was then placed in the experimental box of the scanning transmission X-ray microscope. After pumping out the STXM chamber, it was filled with helium to avoid oxygen contamination. Pristine kaolinite and fine fractions of iron-kaolinite end-products were studied at Fe $L_{2,3}$ -edges and at Al and Si K-edges. Fe-bearing reference minerals with different Fe oxidation states, such as pure ferrous and ferric oxide phases (magnetite, maghemite and goethite) and an iron-rich clay phase (berthierine BStA) were also analyzed at Fe $L_{2,3}$ -edges (see Table 1 for structural formulae).

Data collection

STXM experiments were performed at the spectromicroscopy beamline 10ID-1 at the Canadian Light Source (CLS, Saskatoon) described in detail by Kaznatcheev et al. (2007). This beamline provides an energy range of 130–2,500 eV with a resolving power ($E/\Delta E$) of 3,000. The spatial resolution, driven by Fresnel lenses, is close to 30 nm. This relatively wide energy range and low spatial resolution are especially well suited to our samples as the

principal clay constituents (Al, Si and Fe) could be studied at the particle scale.

The experimental protocols used for STXM data acquisition and analysis can be found in Hitchcock (2001) and Jacobsen et al. (2000). To localize particles, wide field of view images ($100 \times 100 \mu\text{m}^2$) with medium resolution ($1 \mu\text{m}$) were collected at the maximum of Fe absorption (708 eV), to enhance the visualization of Fe-rich particles. These low resolution images were complemented with high-resolution images collected below, around and above the Fe absorption $L_{2,3}$ -edge (700 eV). For microspectroscopy data, stacks of images were collected on a reduced field of view (from 1×1 to $5 \times 5 \mu\text{m}^2$) scanning the sample in the x - y directions at each energy increment over the energy range of interest. At Fe $L_{2,3}$ -edges, each stack was composed of 200 images. Sampling step was set to 0.15 eV in the edge regions. For Al and Si, identical regions of interest were investigated using the same procedure, collecting (1) wide field of view images at the maximum of absorption edge (at 1,572 eV for Al and at 1,844 eV for Si), (2) high-resolution images below and after absorption edge and (3) stacks at Si and Al K-edges (1,835–1,880 and 1,555–1,610 eV respectively).

Data reduction and analysis

The aXis2000 software-package (<http://unicorn.mcmaster.ca>) was used for data and image processing (Hitchcock 2001). Images were re-aligned using the alignment routine of the Stack Analyze program (Jacobsen/Stony Brook, V2.6.1). Transmission images were then converted into optical density (OD) scales according to the following equation: $\text{OD} = -\ln(I/I_0)$ where I_0 represents the incident X-ray flux (a zone outside the sample was selected in each stack to measure I_0) and I represents the measured intensity at the point of interest. Two methods were then employed to extract spectra from stacks. On OD images, Regions Of Interest (ROI) were manually chosen on the basis of the contrast between particles (which depends on sample thickness, iron abundance and status). In the rest of the text, the selected zones will always be referred to as ROIs as opposed to POIs (Points of Interest) selected for micro-XANES investigations. Corresponding spectra were extracted from the stacks using the Zimba tool in aXis2000. Principal component analysis (PCA) with PCA_GUI routine followed by a clustering analysis (Lerotic et al. 2004, 2005) was also used to check that the different possible spectra were well extracted and considered.

A linear background was subtracted from all reference and experimental spectra. Resulting spectra were all normalized setting their area to 1. Reference spectra containing mainly Fe^{2+} were multiplied by 0.8 as a correction factor to take into account the difference in occupancy of the 3d orbitals in Fe^{2+} and Fe^{3+} ions (Van der Laan and

Kirkman 1992). Experimental spectra were fitted with linear combination of normalized reference spectra of one Fe^{2+} phase and one Fe^{3+} phase, applying the CGO (Conjugate Gradient Optimization) curve fit routine in aXis2000. The coefficients thus obtained were used to calculate $\text{Fe}^{2+}:\text{Fe}^{3+}$ ratio in the probed zones.

TEM analyses

TEM analyses were carried out on the same copper grids, using CM20 Philips microscope running at 200 kV. EDX spectra were collected using a Si–Li detector attached to the microscope, with a spot size of about 40 nm and a counting time of 40 s. The resulting signal was analyzed by Spirit software (Princeton Gamma Tech).

Results

Silicon and aluminum K-edges

Bulk XANES, microXANES and STXM analyses at Si and Al K-edges were performed on initial kaolinite, fine (F) and coarse (C) fraction end-products, two Fe-rich clay references (berthierine BStA and chamosite), saponite (Al K-edge only) and complementary reference clays. In that context, it appeared crucial to first describe correctly the status of Al and Si within the initial kaolinite KGa-2.

Initial kaolinite

Figure 1a displays different XANES spectra of KGa-2 kaolinite collected at the (a) Si and (b) Al K-edges. The Si K-edge spectrum of initial kaolinite pressed into pellet displays typical features of clay minerals in which silicon is located in the tetrahedral sheet with the white line maximum intensity at 1,846.8 eV (A) and structures at 1,851.5 (B), 1,857.8 (C), 1,862.3 (D) and 1,866.3 eV (E) (Li et al. 1995a; Shaw et al. 2009). Figure 1a also presents STXM XANES spectra extracted from three distinct particles of kaolinite (few hundreds of nm) (STXM-s1, -s2 and -s3, dotted lines). These spectra display some variations from one spectrum to another in the post-edge region. Especially, the C oscillation is shifted of 2.6 eV for spectrum STXM-s3. The C oscillation is assigned to scattering contributions from atoms of the tetrahedral sheet (Li et al. 1995a). Its variation could then be explained by changes in tetrahedra composition. However, such an explanation appears rather unlikely for a reference clay sample such as kaolinite. Another assumption for the observed changes could be the variations in multiple scattering resulting from different orientations of the clay platelets. The influence of orientation on spectral features was checked by measuring

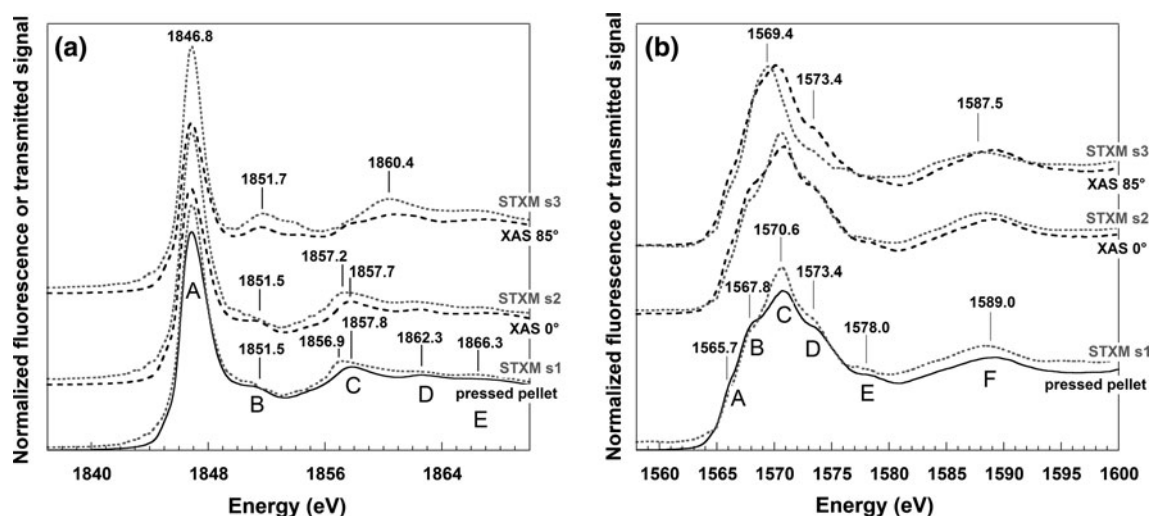


Fig. 1 Comparison of K-edge XAS (solid and dashed lines) and STXM (dotted lines) spectra at Si (a) and Al (b) K-edges. XAS spectra were collected in fluorescence yield mode on a pressed pellet

(solid lines) and on oriented clay films (dashed lines) at angles of 0° (XAS 0°) for normal incidence and 85° (XAS 85°) for grazing incidence

XANES spectra on oriented films using angles of 0° and 85°, corresponding to normal and grazing incidence, respectively (dashed lines in Fig. 1a). Orientation clearly modifies the spectra as compared to the spectrum obtained at 0°; the 85° spectrum exhibits an increase of the B band, whereas the C band broadens and flattens. It must be pointed out that the spectrum of the pressed pellet is similar to that of the 0° oriented film, revealing that compression tends to orientate the particles perpendicularly to the compression axis. It then appears very likely that the variations observed for STXM Si spectra can be assigned to changes in the orientation of clay particles with respect to the incident X-ray beam. This figure also demonstrates the good reliability of STXM data at Si K-edge, and although a lower signal:noise ratio, STXM spectra are well superimposed to XAS spectra.

The Al K-XANES spectrum of initial kaolinite pressed into pellet (Fig. 1b) displays typical features for such 7 Å 1:1 clay mineral in which Al is octahedrally coordinated (Li et al. 1995b; Ildefonse et al. 1998). The following features can be observed: a weak shoulder at 1,565.7 eV (A), followed by a stronger component at 1,567.8 eV (B) in the edge region. The white line maximum position is at 1,570.6 eV (C). In the post-edge region, two broad components occur at 1,573.4 eV (D) and 1,578 eV (E), respectively, whereas the first EXAFS oscillation is at 1,589 eV (F). The relative intensities of the different A to D structures depend on site geometry and local structure (Ildefonse et al. 1998; Li et al. 1995b). Al K-edge spectra extracted from the STXM ROIs (STXM-s1, -s2 and -s3) display the same trend, although less dramatic, as for Si K-edge. Indeed, the first two spectra appear rather well superimposed to the reference spectra obtained for pressed

pellet and oriented film at 0°, respectively. The latter (s3) differs from the other STXM spectra due to the absence of the shoulder B at 1,568 eV and a slight shift of both white line C and first oscillation F. The structures B and E are hardly detected on the Al K-edge spectrum of oriented film at 85°. These observations strongly suggest that, as for Si K-edge, variations in the shape of Al K-edge STXM spectra for kaolinite are due to particle orientation effects.

Iron-kaolinite reaction end-products

Si K-edge, bulk and micro-XANES Figure 2a displays the bulk Si K-edge XANES spectra obtained on pure KGa-2 kaolinite, and F and C fractions, together with spectra obtained with a micrometric beam on various POIs defined from XRF maps (not shown). Only marginal variations can be observed between these various spectra. Still, all reaction products display a flatter oscillation C. Such an evolution could be linked to changes in multiple scattering resulting from orientation differences (Briois et al. 2007), to a loss of order as observed on a series of synthetic allophane materials (Vantelon and Montargès-Pelletier, personal communication) or to variations in tetrahedral and octahedral sheets composition (nature of atoms and filling ratio).

In any case, as evidenced from Fig. 2b, none of the obtained spectra corresponds to either chamosite or berthierine. Indeed, the spectra of these two minerals present a significant shift of the C resonance toward lower energies that is never observed in the spectra of the reaction products. Such a shift may be tentatively assigned to increasing substitution in the tetrahedral sheet. Indeed, the spectra in Fig. 2b display a correlation between the amount of

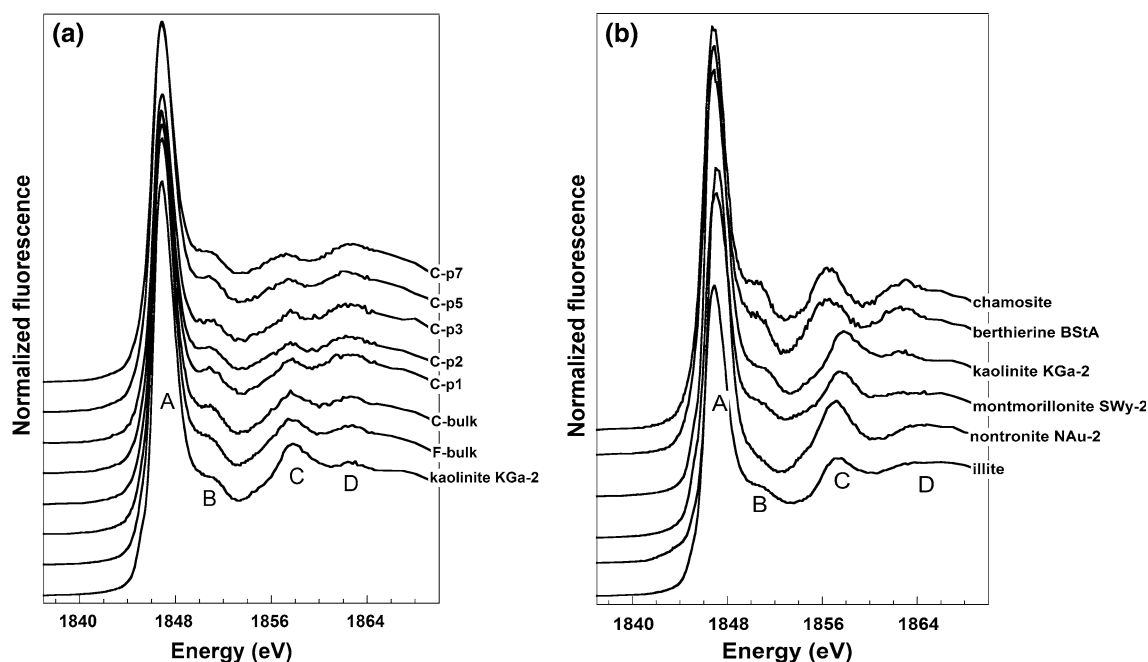


Fig. 2 Si K-edge XANES. **a** Fine (*F*) and coarse (*C*) fractions in bulk mode, selected POI's, **b** clay references

tetrahedral substitution (Table 1) and the position of the C resonance. The spectrum corresponding to SWy-2 montmorillonite with low Al for Si substitution (tetrahedral substitution rate (x_t) equal to 0.0325) is close to that of kaolinite whereas that of illite displays a C resonance at an intermediate position between kaolinite and chamosite or berthierine, in agreement with the moderate substitution rate in the tetrahedral sheet (x_t equal to 0.1125). However, this shift can also be due to the difference of composition of layer for each presented clay mineral, and the number and nature of second neighbors could provide another interpretation of Si K-edge spectra. Indeed, chamosite and berthierine are both trioctahedral clay minerals and Fe-rich minerals, suggesting a stronger contribution of second neighbors scattering. This second assumption is supported by the position of the feature C for nontronite which is a Fe-rich dioctahedral clay mineral. Further investigations involving well-characterized clay minerals with close layer composition should help for the assignment of this shift toward lower energies.

STXM experiment at Si K-edge Figure 3 displays X-ray transmission images at Si, Al and Fe edges for a 15- μm large aggregate of particles. The right image is an OD image below the Fe L_3 -edge of an enlargement of a selected area. Figure 4 presents another studied area, also analyzed by TEM, that displays a relatively lower Fe content.

Si K-edge spectra extracted from ROIs of Figs. 3 and 4 are plotted in Fig. 5. Due to the decrease of signal:noise

ratio related to the investigations at a nanoscale level, the quality of these spectra is lower than those of spectra acquired in bulk and micro-beam modes (Fig. 2). Indeed, the signal:noise ratio of spectra depends on the thickness of clay particles and their content in Si. Although some spectra display distortions in the pre-edge region, those anomalies are low in intensity and do not affect the higher energy range of the spectra. Significant information can be obtained from this set of spectra. For both zones (stacks I and II), the spectra display significant variations from one ROI to another in contrast with the low variability observed on bulk and micro-beam XANES spectra. Some of these variations can clearly be assigned to orientation effects, especially when the spectra flatten in the post-edge region. Some others, for instance in z3 and zH, suggest structural changes. Still, the most important information brought by these data is that no spectrum can be assigned to berthierine whose signal presents a significant shift of structure C toward low energy and spectra remain rather close to that of initial kaolinite. These spectra clearly demonstrate that there is no individual particle of berthierine-like minerals, and that kaolinite fingerprint predominates for any investigated particles.

Al K-edge, bulk and micro-XANES At the Al K-edge, spectra of all reaction products and POI's display significant evolution in comparison with the spectrum of initial kaolinite (Fig. 6a). Indeed, an increase in the low energy feature at 1,566 eV can be observed together with an attenuation of structure D, a disappearance of structure E,

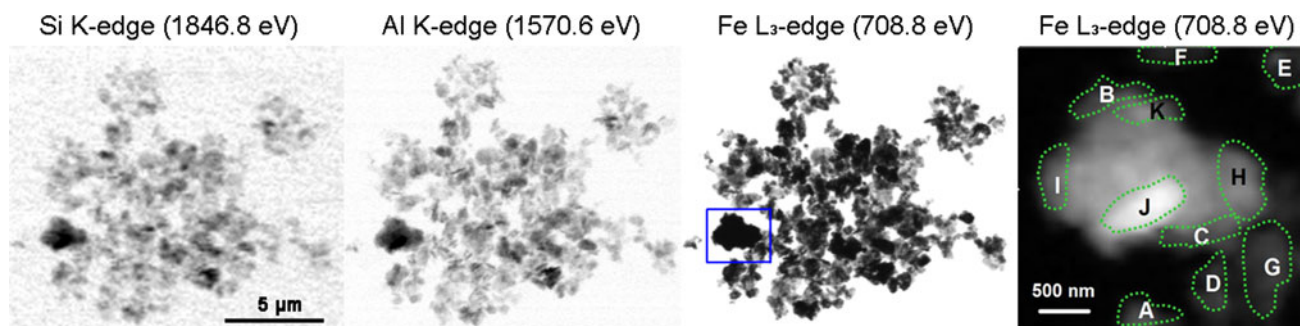


Fig. 3 STACK I. Si and Al K-edges, Fe L_3 -edge transmission maps of a clay particles aggregate and Fe L_3 -edge optical density map enlargement

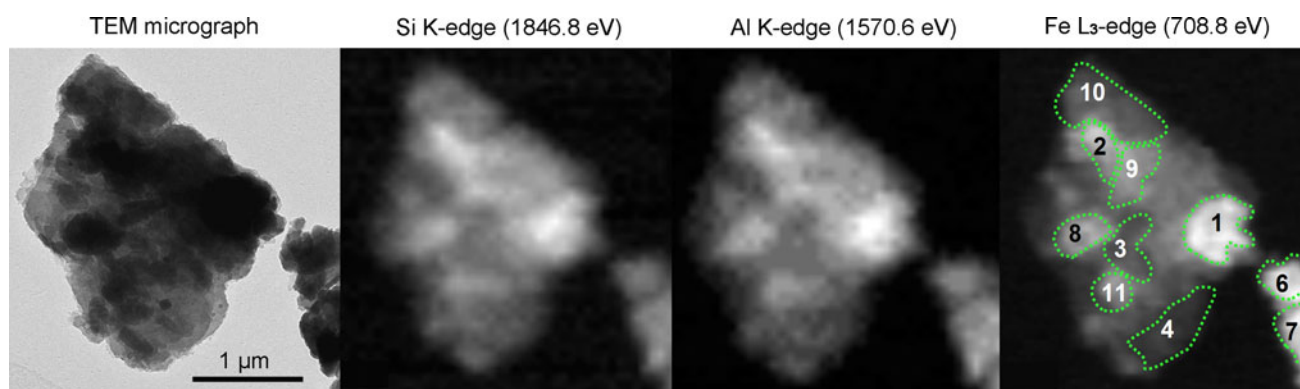


Fig. 4 STACK II. TEM micrograph, Si and Al-K edges and Fe L_3 -edge optical density maps of clay particles

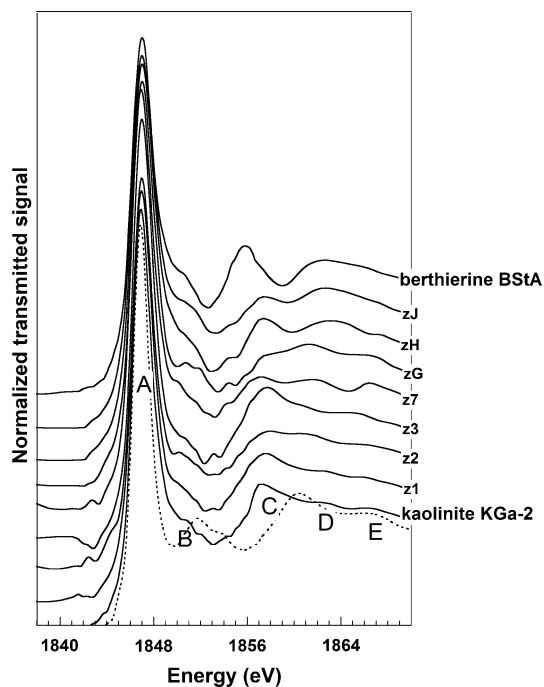


Fig. 5 STXM Si K-edge spectra of selected zones of STACK I and II (Figs. 3, 4) compared to spectra of initial kaolinite KGa-2 and berthierine BStA. The two spectra of kaolinite KGa-2, in *solid* and *dashed* lines, are STXM-s1 and STXM-s3, respectively, on the Fig. 1a

and a shift of oscillation F toward lower energy. The signal at 1,566 eV is classically assigned to tetrahedral aluminum (^{IV}Al) (Ildefonse et al. 1998; Li et al. 1995b). This is confirmed by the spectra obtained for pure saponite, a mineral that contains ^{IV}Al only (Fig. 6b; Table 1) and for SWy-2 montmorillonite, that is almost devoid of ^{IV}Al . Further confirmation of this assignment is provided by the spectra of phyllosilicates with mixed coordination of aluminum (^{IV}Al and ^{VI}Al) such as chamosite, berthierine BStA, and nontronite NAu-2, that present a clear shoulder at 1,566 eV. The intensity of this shoulder follows the ^{IV}Al : ^{VI}Al ratios of these minerals (Table 1).

The global evolution of the Al K-edge spectra after reaction between kaolinite and metallic iron could be interpreted as corresponding to the formation of berthierine, as the spectral features observed tend those of pure berthierine (Fig. 6b). Still, the global shape of the spectra is not exactly similar to that of pure berthierine, which strongly suggests that the actual reaction products are rather mixtures of berthierine and kaolinite, an assumption that was already proposed on the basis of global analyses (Rivard et al. 2013).

To test such a scenario, we tried to reproduce the spectra of the reaction products by a linear combination of

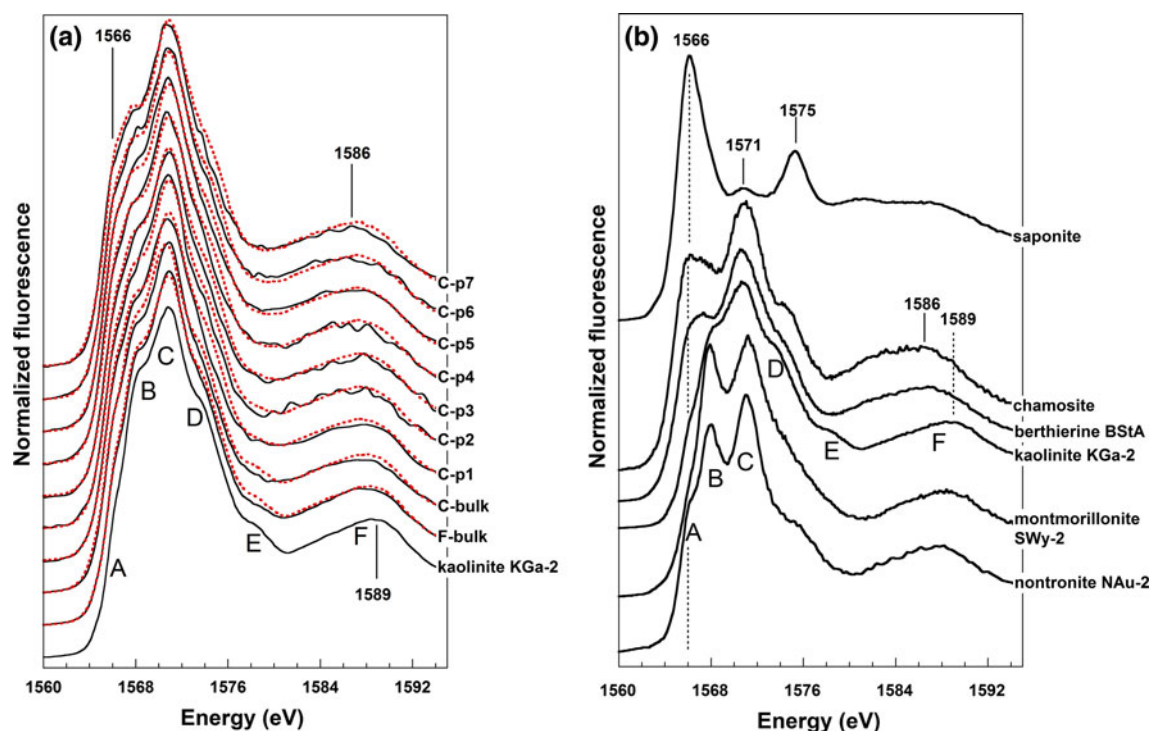


Fig. 6 **a** Al K-edge XANES spectra (*solid lines*) and linear combination fits (*dashed lines*) for kaolinite-iron end-products, fine (*F*) and coarse (*C*) fractions in bulk mode, POIs (*curves P1 to P7*), KGa-2 spectrum was

plotted against those *curves* for comparison. **b** Al K-edge XANES spectra of reference samples: saponite, chamosite, berthierine BSTa, kaolinite KGa-2, montmorillonite SWy-2 and nontronite NAu-2

kaolinite and berthierine spectra. Spectra were normalized in order to get free of the influence of Al content on fluorescence intensity, and normalization was operated on the basis of the height of the most intense structure at 1,571 eV. As shown in Fig. 6a, such a procedure provides very satisfactory fits that are able to reproduce the features of all the spectra of the reaction products. For the various POIs as well as for the *C* and *F* fractions, it provides relative proportions of both phases in the probed aggregate (Table 2). It appears that for all POIs, the calculated proportion in berthierine is rather high, ranging between 61 and 83 %. Such high values likely result from the fact that the POIs were selected for their high content in Fe. Accordingly, results obtained for the bulk samples reveal lower contents in berthierine. In those latter samples, the coarse fraction exhibits a significantly higher berthierine content, in agreement with SEM observations showing remaining metallic iron grains coated by Fe-rich clay particles (Rivard et al. 2013). From the obtained linear combination coefficients of berthierine and kaolinite and considering $^{IV}Al:^{VI}Al$ ratio of 1 and 0.04 for berthierine and kaolinite respectively, the global $^{IV}Al:^{VI}Al$ ratio could be determined in each investigated point. Following the berthierine abundance, these ratios take values between

0.32 and 0.58 for POI's and are lower for bulk analyses (0.13 and 0.21 for *F* and *C* fractions, respectively).

In any case, results obtained by Al K-edge absorption spectroscopy clearly confirm the formation of a system of mixed aggregates. The mixtures are formed by initial kaolinite and an Fe-rich clay phase with a structure related to that of berthierine. Still, as the spatial scale probed by micro-beam XAS remains higher than that of the individual particles, it is relevant to analyze the samples using a higher resolution by STXM.

STXM experiment at Al K-edge Some typical Al K-edge spectra extracted from stack I and II (Figs. 3, 4) are presented on Fig. 7 and compared to initial kaolinite and berthierine spectra (STXM data). For end-products (curves zG, zJ and z1), a broadening of the edge jump on the low energy side is clearly visible revealing the presence of ^{IV}Al for all the particles. This feature appears more intense for the zones richer in Fe (Figs. 3, 4). Still, none of the observed spectra can be assigned to pure berthierine, no ^{IV}Al -free particle is detected, and all particles provide the fingerprint of ^{VI}Al which shows that even at the scale probed by STXM, the particles resulting from the reaction of kaolinite with Fe are intimate mixtures of kaolinite and a berthierine-like phase.

Table 2 Al K-edge XANES linear combination fitting parameters

POI	LCF coefficients (%)		R-factor (10 ⁴)	χ_r^2 (10 ⁴)	Al ^{IV} :Al ^{VI}
	Kaolinite KGa-2	Berthierine BStA			
P1	47	53	16	62	0.32
P2	46	54	15	51	0.33
P3	44	56	12	38	0.35
P4	34	66	12	40	0.44
P5	30	70	11	43	0.48
P6	29	71	10	41	0.50
P7	22	78	13	53	0.58
F	79	21	6	23	0.13
C	64	36	11	43	0.21

Al^{IV}:Al^{VI} ratio is equal to 1 for berthierine BStA and to 0.04 for kaolinite KGa-2

Iron edges

Bulk and Micro-XANES at Fe K-edge

In order to get relevant information on Fe status within neoformed clay minerals, XAS experiments were carried out as they allow distinguishing metallic iron from Fe located inside clay mineral phases or within Fe oxyhydroxides. Bulk XAS experiments were carried out on the *F* fraction only as in the *C* fraction, the high metallic iron

content dominates the Fe signal, preventing a proper analysis of Fe status. Figure 8a presents normalized micro-XANES spectra collected at the Fe K-edge for different POIs sampled in both the *C* and *F* fractions, together with bulk-XANES spectra obtained for the *F* fraction and various reference samples (magnetite, illite, berthierine BStA and chamosite). The edge position and shape of all reaction products are close to those observed for pure berthierine BStA that contains mainly ^{VI}Fe²⁺. Still, differences can be noticed as the signal of berthierine BStA exhibits a more pronounced broad oscillation at 7,143.5 eV compared to the investigated products. The pre-edge position and shape (Fig. 8b) suggest that Fe is mainly octahedrally coordinated (Wilke et al. 2001; Farges et al. 2004). The observed variations in white line intensity can likely be assigned to self-absorption effects due to variations in Fe concentration. Still, for several investigated points of the *C* fraction, the spectra exhibit a drastic increase in the pre-edge region, associated with an apparent broadening of the white line and a decrease of the white line intensity (C-p12 and C-p11). Such features can be assigned to the presence of metallic iron in the investigated points, as confirmed by EXAFS curves on the same POIs (not shown). Then, for these spectra, the examination of pre-edge region for the determination of oxidation state of Fe was not possible. At the aggregate scale, it was not possible to distinguish different oxidation states of Fe. The differences observed are mainly due to the presence of metallic iron in the investigated aggregates.

EXAFS experiments at Fe K-edge

Figure 9 displays EXAFS oscillations (a) and corresponding Fourier transforms obtained at the Fe K-edge (b), in bulk for the *F* fraction, berthierine BStA and chamosite, and for POI F-p2.

The EXAFS spectra collected for all points whether in bulk or with micro-beam are rather similar. The local environment around Fe in reaction products appears to be close to that in chamosite or berthierine BStA. It must be pointed out that the EXAFS signals of these two minerals are rather similar despite their crystal chemistry differences. Indeed, in chamosite Fe atoms have four tetrahedral neighbors at 3.35 Å, whereas in berthierine, they only have two. This reveals that the backscattering signal resulting from these atoms is rather weak and does not strongly contribute to the whole EXAFS signal.

In contrast, as shown by the previous studies on Fe K-edge EXAFS of clay minerals (Vantelon et al. 2003), the signals are extremely sensitive to the distribution of Fe within the octahedral sheet. The first and second peak of the Fourier transform magnitude (Fig. 9b) can then be fitted by considering only four shells: two sub-shells of

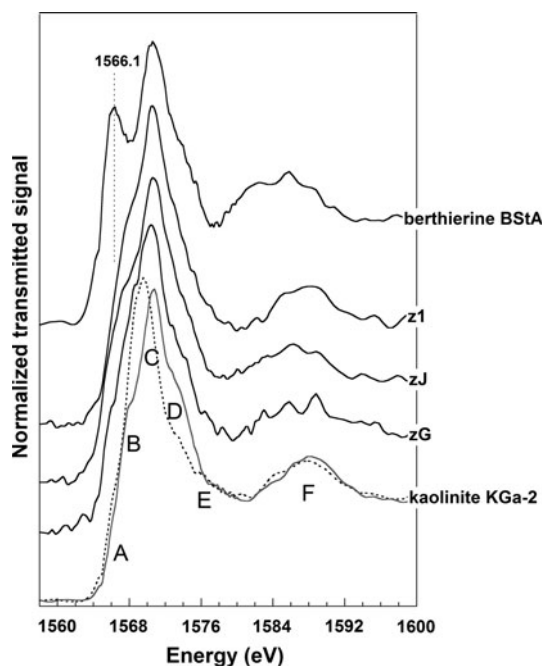


Fig. 7 STXM Al K-edge spectra of selected areas of the stacks I and II (Figs. 3, 4) compared with initial kaolinite KGa-2 and berthierine BStA reference spectra. The two spectra of kaolinite KGa-2, in *solid* and *dashed* lines, are STXM-s1 and STXM-s3, respectively, on the Fig. 1b

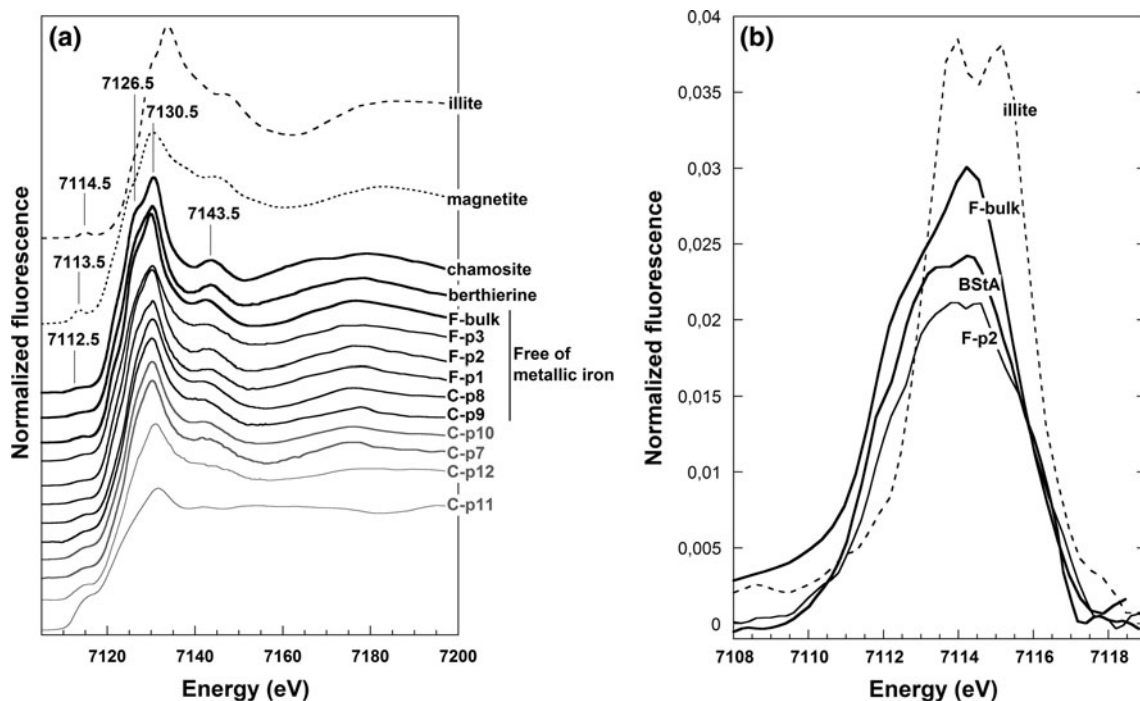


Fig. 8 a Fe K-edge XANES spectra collected at POI's for fine fractions (*F*) and in bulk mode for fine fraction (*F*), berthierine BStA, chamosite, magnetite and illite reference samples. b Pre-edge peaks for illite, fine fraction, berthierine BStA and POI F-P2

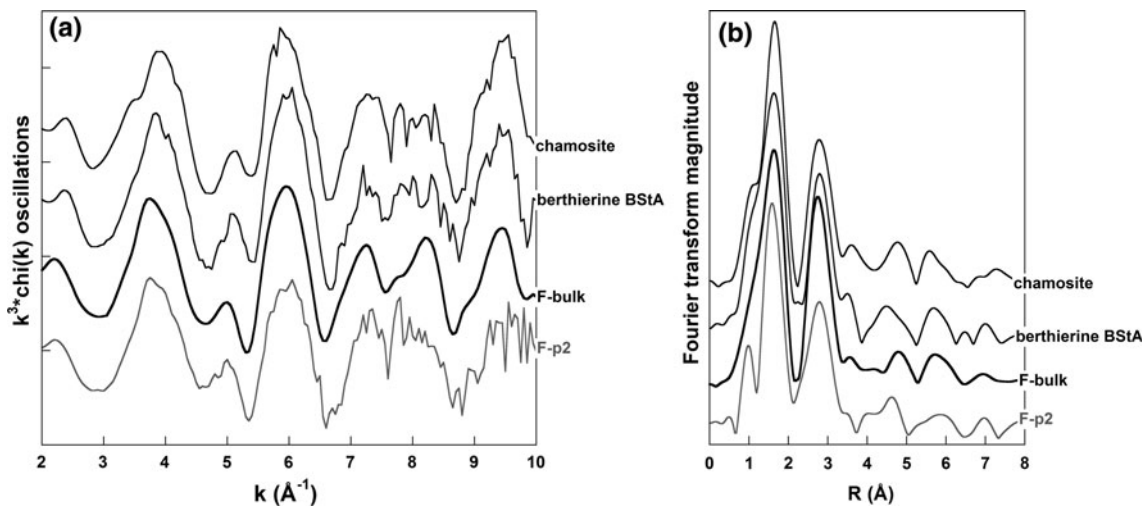


Fig. 9 EXAFS oscillations (a) and corresponding Fourier transform (b) for POI F-P2 and bulk mode data for fine fraction (*F*), berthierine BStA and chamosite

oxygen atoms, one of octahedral cations surrounding the central Fe atoms, two Si atoms from the tetrahedral sheet and oxygen atoms of the neighboring octahedra. As shown in Fig. 10, very satisfactory fits of the experimental data can indeed be obtained with those four shells. In the present case, the fits were obtained by considering only Fe neighbors in the octahedral sheet. It then confirms that the newly formed Fe-rich clay minerals have an octahedral sheet formed with Fe atoms. Finally, the number of Fe

neighbors deduced from the fit is around 5 (Table 3). It shows that the newly formed products are mostly trioctahedral (6 Fe²⁺ neighbors) with possibly a few dioctahedral domains (3 Fe³⁺ neighbors). It is then highly relevant to probe the oxidation state of Fe at the particle scale using STXM experiments, as the L-edge is much more sensitive to oxidation state (Van der Laan and Kirkman 1992). The presence of Fe³⁺ cannot be fully excluded on the basis of experiments at the Fe K-edge.

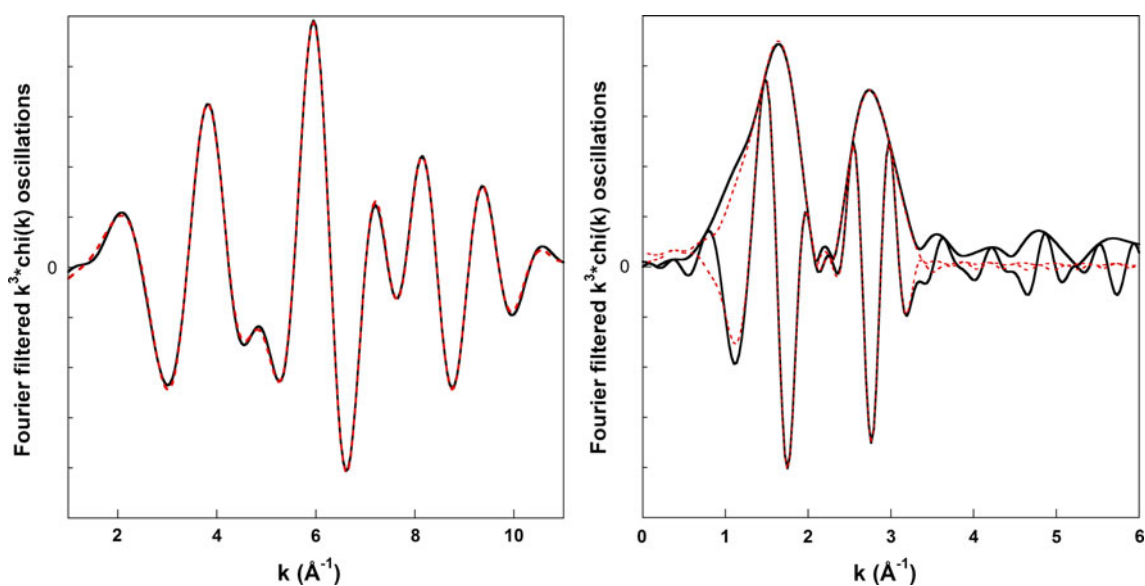


Fig. 10 Fourier-filtered EXAFS oscillations, Fourier transform magnitude and imaginary parts (*solid lines*) and fitting curves (*dashed lines*) for the fine fraction

Fe oxidation state at particles scale: STXM experiments

Reference spectra The X-ray absorption spectra of 3d transition metals, such as Fe, display $L_{2,3}$ -edges dominated by dipole transitions from the core 2p level to the empty 3d states. Due to the strong Coulombic interactions between these two levels, those transitions are strongly linked to the local electronic structure. Studying $L_{2,3}$ -edge spectra can then provide information about the oxidation state and symmetry of 3d transition metals (Van der Laan and Kirkman 1992; Crocombette et al. 1995; Van Aken and Liebscher 2002; Calvert et al. 2005). Figure 11 presents Fe L-edge spectra collected for pure and mixed valence compounds. Berthierine BStA is a pure valence compound, constituted of Fe^{2+} in octahedral symmetry. The corresponding Fe L-edge spectrum present two massives at the L_3 ($2p_{3/2}$) and L_2 ($2p_{1/2}$) edges, with large splitting of the lines at both edges, induced by crystal field and spin-orbit effects. The global shape can be compared to other Fe L-edge spectra obtained for Fe^{2+} -oxides (Crocombette et al. 1995; Wasinger et al. 2003; Miot et al. 2009). The L_3 line shows a complex splitting with two lines close in intensity and satellite components on both low and high energy sides. The spectrum corresponding to berthierine is markedly distinct from those of compounds that contain Fe^{3+} only such as maghemite and goethite. Both compounds display rather similar spectra with marginal differences in the shape of the L_3 line, indicative of the fact that in goethite, only ^{VI}Fe is present whereas maghemite contains both $^{IV}Fe^{3+}$ and $^{VI}Fe^{3+}$. The spectrum of magnetite, a mixed valence compound with three different sites

for Fe (one-third of $^{IV}Fe^{3+}$, one-third of $^{VI}Fe^{3+}$ and one-third of $^{VI}Fe^{2+}$), displays features and line positions that are intermediate between goethite and berthierine, which shows the extreme sensitivity of Fe $L_{2,3}$ spectra to oxidation state.

Iron-kaolinite reaction end-products Figure 12 displays the spectra extracted from stack I (Fig. 3). In the L_3 edge region, all spectra display an intense peak at 708.6 eV and a less intense peak at 710.6 eV, indicating that most Fe is under a ferrous state. However, the intensity ratio between the two main peaks appears to slightly vary from one spectrum to another, which suggests variations in $Fe^{2+}:Fe^{3+}$ ratios. $Fe^{2+}:Fe^{3+}$ ratios can be quantitatively determined by fitting experimental spectra as a linear combination of spectra of compounds containing only Fe^{3+} and Fe^{2+} provided the crystal chemistry is somehow similar. In the present study, we chose to use berthierine BStA as the Fe^{2+} reference and goethite as the Fe^{3+} reference. The use of goethite as Fe^{3+} reference was validated as similar results were obtained using ferrihydrite and hematite reference spectra, providing close $Fe^{2+}:Fe^{3+}$ ratios at $\pm 1\%$. Such a procedure provides good quality fits (Fig. 12) that reveal Fe^{2+} contents ranging between 72 and 81 %.

On the second aggregate of clay particles (Fig. 4, STACK II), the set of extracted spectra from the stack can all be fitted using the same two pure components (Fig. 13). Still, the distribution of Fe oxidation state appears more heterogeneous than in the previous stack as the percentages in Fe^{2+} go between 54 and 80 %. The same region was studied using TEM-EDXS, in order to complement

Table 3 Fitting parameters for EXAFS data of fine fraction

1st coordination sphere			2nd coordination sphere						R factor			
O	R	σ^2	Fe	R	σ^2	Si	R	σ^2		O	R	σ^2
2	1.980	0.0062	5	3.163	0.0087	2	3.216	0.0033	2	3.546	0.0028	0.0016
4	2.127	0.0052										

Amplitude factor $S_0^2 = 0.7$, energy shift $\Delta E = -3$ eV

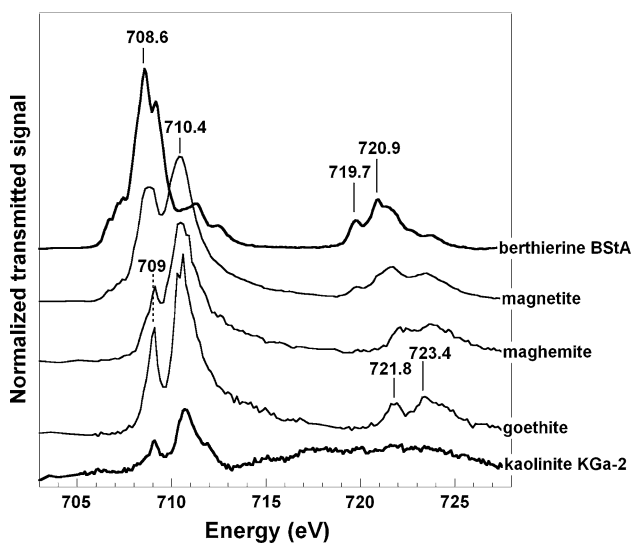


Fig. 11 Fe $L_{2,3}$ -edges XANES spectra of initial kaolinite and reference minerals with variable $Fe^{2+}:Fe^{3+}$ ratio: goethite, maghemite, magnetite and berthierine BStA

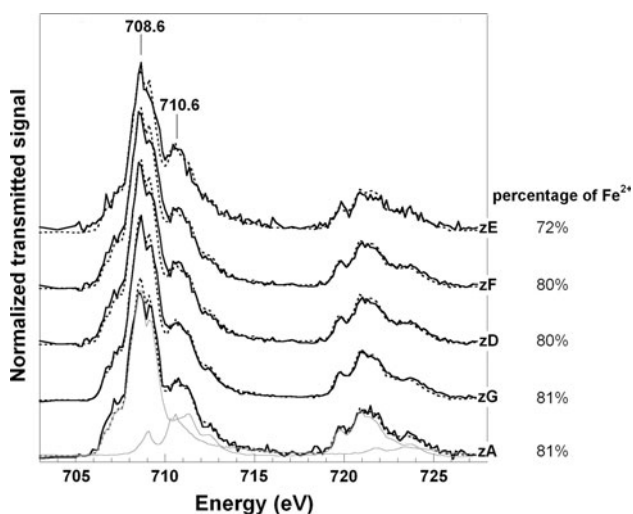


Fig. 12 Fe $L_{2,3}$ -edges XANES spectra (solid black lines) obtained from zones described on Fig. 3. Each spectrum area is normalized to 1. Linear combinations (dashed lines) of normalized spectra of berthierine BStA and goethite (solid gray lines) yield the ferrous iron percentages

oxidation state information with Fe content distribution for all the investigated particles. As a general trend, Fe content increases with increasing Fe^{2+} percentage (Fig. 14). Such a

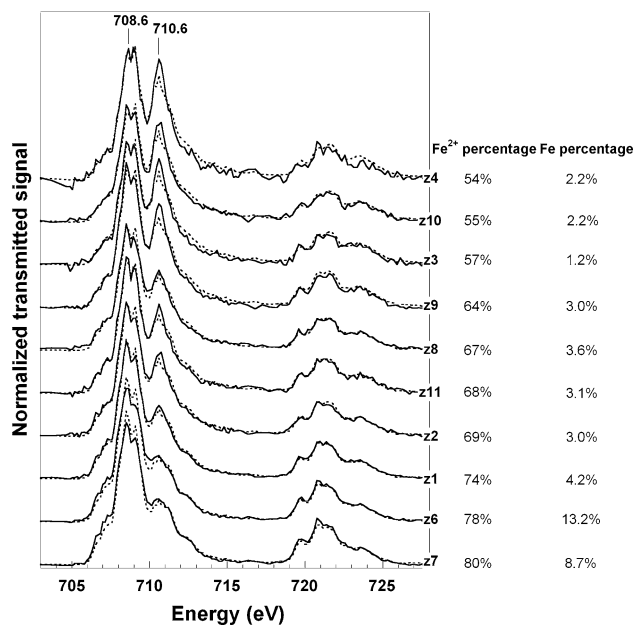


Fig. 13 Fe $L_{2,3}$ -edges XANES spectra (solid lines) obtained from zones described on Fig. 4. Each spectrum area is normalized to 1. Linear combinations (dashed lines) of normalized spectra of berthierine BStA and goethite yield the ferrous iron percentages. Iron atomic percentages were obtained for the same regions using TEM-EDXS

trend was confirmed by analyses of additional regions (not shown) by combined STXM and TEM-EDXS.

Discussion

According to our previous study, the reaction products obtained after contacting pure kaolinite with metallic iron powder in anoxic conditions at 90 °C were mainly intimate mixtures between initial kaolinite and newly formed berthierine (Rivard et al. 2013). The present detailed spectroscopic investigation confirms such a scenario by revealing mixed signals in all the investigated Fe-rich points, whatever the observation scale. The spectra obtained at the Si and Al K-edges are consistent with the formation of berthierine as (1) the local environment of Si in the mixed particles is modified and (2) the presence of ^{IV}Al is evidenced. Still, as the proportion of ^{IV}Al and ^{VI}Al vary significantly between particles, it is impossible to ensure that the newly formed Fe-rich clay phase is devoid of ^{VI}Al .

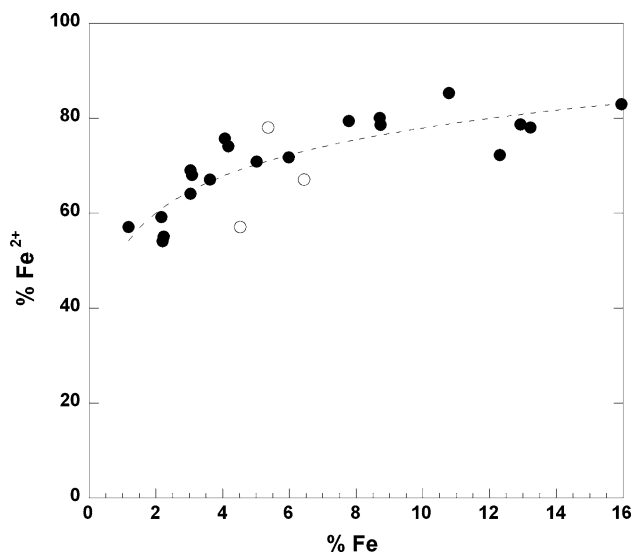


Fig. 14 Variations of Fe^{2+} proportion with total Fe content at the particle scale (filled circles, provided by STXM data and TEM-EDXS analyses) and at the bulk scale (empty circles, Mössbauer spectroscopy data from Rivard et al. 2013)

Data obtained at the Fe edges provide further information. Indeed, they show that Fe is octahedrally coordinated and likely clustered in octahedral sheets whose structure is mainly trioctahedral. However, variable $\text{Fe}^{2+}:\text{Fe}^{3+}$ ratios are observed in different particles, which unambiguously reveals that the crystal chemistry of the newly formed Fe-rich phases is not unique and can vary from one particle to another. In the following sections, we will use all the experimental data obtained so far to determine possible crystal structures in the reaction products.

In order to determine unit cell compositions, elementary analyses obtained by TEM-EDXS are combined with the $\text{Fe}^{2+}:\text{Fe}^{3+}$ ratios provided by STXM experiments (Table 4). The basic assumption underlying the calculation are (1) all particles are mixtures of initial kaolinite and Fe-rich sub-particles; (2) Al can be located in either tetrahedral or octahedral sheets; (3) Fe is octahedral whatever its oxidation state. In the following section, the formed minerals are assumed trioctahedral only. Calculations for dioctahedral domains are presented in On line Resource. Assuming that the newly formed Fe-rich clay phases are close to theoretical berthierine, their unit cell formula can be written as:



where x is the substitution rate in tetrahedral sheets and u and t are Fe^{3+} and Al^{3+} substitutions in octahedral sheets, respectively. As electrical neutrality must be ensured,

$$u = x - t.$$

Unit cell formula of Fe-rich layers for each mixed particle can then be obtained from the determination of x , u

Table 4 TEM-EDXS chemical compositions of clay particles (atomic percentage) and corresponding $\text{Fe}^{2+}:\text{Fe}^{3+}$ ratio determined by STXM

	1a	3a	4a	6a	7a	8a	9a	10a	11a	1b	2b	3b	4b	5b	6b	7b	8b	9b	10b
Al	16.57	17.75	16.75	12.97	13.52	16.43	17.68	16.93	16.47	15.16	11.72	12.19	10.86	13.61	12.88	14.46	14.72	11.73	14.40
Si	14.88	15.70	14.39	12.42	13.40	14.95	15.48	15.43	15.12	17.77	11.24	12.34	8.95	13.58	12.23	16.22	15.16	12.39	15.83
Fe	4.17	1.18	2.20	13.23	8.71	3.62	3.04	2.24	3.08	2.17	12.93	10.79	15.96	7.79	8.74	4.07	5.02	12.31	5.98
$\text{Fe}^{2+}:\text{Fe}^{3+}$	2.85	1.33	1.17	3.55	4.00	2.03	1.78	1.22	2.13	1.45	3.68	5.79	4.85	3.85	3.66	3.12	2.42	2.60	2.54

Points of analyses with the a letter correspond to the points recorded on the STACK II (Figs. 4, 13); b analyses correspond to additional investigation regions

Table 5 Berthierine structural formula and percentage and Al^{IV}:Al^{VI} ratio in kaolinite-berthierine mixed particles, based on TEM-EDXS and STXM analyses

	6a	7a	2b	3b	4b	5b	6b	8b	9b	Mean values	SD
Tetrahedral											
Si	1.17	1.17	1.11	1.22	1.09	1.16	1.09	1.15	1.12	1.14	0.04
Al	0.83	0.83	0.89	0.78	0.91	0.84	0.91	0.85	0.88	0.86	0.04
Octahedral											
Fe ²⁺ Tri	2.17	2.17	2.11	2.22	2.09	2.16	2.09	2.15	2.12	2.14	0.04
Fe ³⁺ Tri	0.59	0.50	0.56	0.36	0.43	0.51	0.53	0.77	0.79	0.56	0.14
Al Tri	0.24	0.33	0.33	0.42	0.48	0.34	0.38	0.08	0.09	0.30	0.14
Berthierine (wt %)	64	48	69	61	89	44	51	26	61	57	18
Al ^{IV} :Al ^{VI} in mixed particles	0.50	0.28	0.60	0.39	1.15	0.25	0.34	0.14	0.50	0.46	0.29

and *t* and of kaolinite (κ) and berthierine (β) proportions in the mixed particle. The kaolinite unit cell used in the calculation is based on the formula proposed by Mermut and Cano (2001), taking into account Si, Al and Fe only, while neglecting minor elements such as Ti, Ca, Na and K. If a mixed particle is formed with κ half unit cells of kaolinite and β half unit cells of berthierine, a matrix equation $E = M \times R$ can be written where E is the vector of elemental compositions in atomic percentage, R the vector of unknown parameters and M the composition matrix:

$$\begin{bmatrix} Si \\ Al \\ Fe^{3+} \\ Fe^{2+} \end{bmatrix} = \begin{bmatrix} 1.99 & 2 & -1 & 0 \\ 1.98 & 0 & 2 & -1 \\ 0.03 & 0 & 0 & 1 \\ 0 & 3 & -1 & 0 \end{bmatrix} \times \begin{bmatrix} \kappa \\ \beta \\ \beta x \\ \beta t \end{bmatrix} \quad (1)$$

By inverting this square matrix, values for κ , β , βx and βt can be obtained, which consequently provides values for x and t that are then used to derive unit cell compositions for each data set. It must be pointed out that, using such a procedure, meaningful results are obtained only for particles with Fe contents higher than 5 % that are also the most concentrated in Fe²⁺ (Fig. 14). Only those results are then presented in Table 5. Those particles display a rather high berthierine proportion (>26 % with a mean value of 57 wt%). The tetrahedral substitution rates of the newly formed berthierine all lie in a narrow range (0.83–0.91) which is consistent with berthierine crystal chemistry. These values are, however, slightly higher than those reported by Brindley (1982) (0.46–0.85). ^{VI}Al accounts for around 10 % of the octahedral composition. Such low values agree with EXAFS modeling that showed that Fe–Al pairs were negligible. In addition, ^{IV}Al:^{VI}Al ratios can be calculated for each particle. The obtained ratios lie between 0.15 and 0.60 (Table 5), which concurs with the values determined by fitting XANES spectra (Fig. 6a; Table 2).

The composition of all the samples displayed in Table 5 can be plotted in a ^{VI}Fe²⁺–^{VI}Fe³⁺–^{VI}Al ternary diagram and compared with compositions from the literature

(Fig. 15). It clearly appears that the compositions of the Fe-rich clays formed by the reaction between kaolinite and metallic iron are located between the pole of berthierine (Brindley 1982) and that of greenalite-cronstedtite. Indeed, in comparison with the berthierine pole, these samples are richer in Fe³⁺ and poorer in ^{VI}Al. This can be linked to the formation mechanism of these Fe-rich clays. As there are tetrahedral substitutions in berthierine and so less Si per tetrahedron in comparison with kaolinite, a higher number of tetraedra could be formed in comparison with the initial one in kaolinite, with the same quantity of Si atoms. As no ^{IV}Fe is observed, and considering the high ^{IV}Al:^{VI}Al ratio

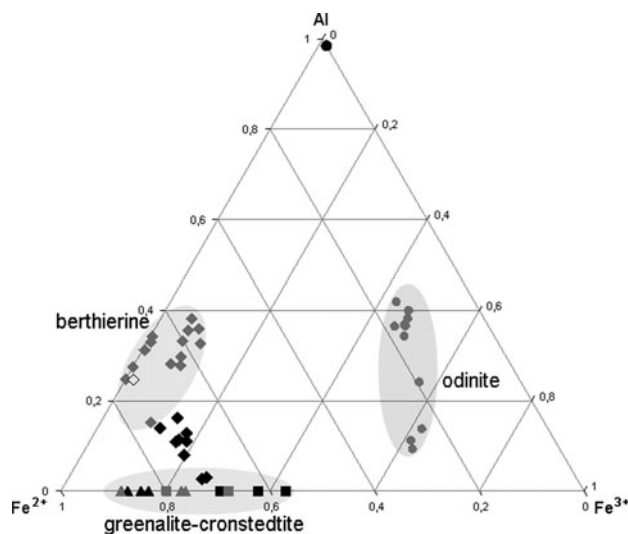


Fig. 15 Chemical composition of the octahedral sheet of the clay particles in a Al³⁺–Fe³⁺–Fe²⁺ ternary diagram. Initial kaolinite is represented by the black circle, calculated composition of berthierines (without octahedral domains) by black diamonds, cronstedtites by black triangles and greenalite by black squares. Literature references are represented by gray symbols: diamonds for berthierine (filled, for Brindley 1982 or empty for berthierine BStA), circles for odinite (Bailey 1988), triangles for cronstedtite (Geiger et al. 1983; Kogure 2002) and square for greenalite (Guggenheim and Bailey 1989; Devaraju et al. 2000)

Table 6 Cronstedtite and greenalite structural formula and percentages, based on TEM-EDXS and STXM analyses

	Cronstedtites						Greenalites				
	1a	8a	11a	7b	Mean values	SD	4a	9a	10a	Mean values	SD
Tetrahedral											
Si	1.62	1.50	1.54	1.65	1.58	0.07	2.00	2.00	2.00	2.00	0.00
Fe ³⁺	0.38	0.50	0.46	0.35	0.42	0.07	–	–	–	–	–
Octahedral											
Fe ²⁺ Tri	2.62	2.50	2.54	2.65	2.58	0.07	1.41	1.81	1.57	1.60	0.20
Fe ³⁺ Tri	0.38	0.50	0.46	0.35	0.42	0.07	–	–	–	–	–
Fe ³⁺ Di	–	–	–	–	–	–	1.06	0.79	0.95	0.93	0.13
Newly formed 7 Å (wt %)	18	15	13	18	16	2	14	16	12	14	2

suggested by Al XANES, it can be proposed that ^{IV}Al from starting kaolinite is mobilized mainly to form these additional tetrahedra (^{IV}Al) in berthierine. The resulting charge deficit is then compensated by ^{VI}Al in low amount and Fe³⁺. In summary, the newly formed Fe-rich clays display a tetrahedral composition corresponding to berthierine but octahedral compositions that lie in between those of berthierine and of greenalite-cronstedtite.

In view of these results, the fact that the composition of the particles with lower Fe content could not be determined following Eq. 1 could suggest the presence in those particles of other Fe-rich clay phases. Such an assumption is further supported by two facts: (1) Al:Si ratios in these particles are systematically lower than in Fe-rich particles (Table 4) indicating an Al deficit in comparison with initial kaolinite; (2) the Fe²⁺:Fe³⁺ ratio obtained on bulk sample by Mössbauer analysis (Rivard et al. 2013) is clearly lower (69:31) than that derived from the berthierine mean formula (79:21, Table 5). The relatively low Al:Si ratios bring us to try to interpret the composition of these Fe-poor particles as mixtures of kaolinite with cronstedtite or greenalite, two Fe-serpentine that do not contain any Al. On the basis of the following unit cell formulae of cronstedtite γ : (Si_{2-x}^{IV}Fe_x³⁺Si_{2-x}^{IV}Fe_x³⁺) (^{VI}Fe_{3-x}²⁺^{VI}Fe_x³⁺) O₅(OH)₄ and of greenalite ϕ : Si₂(^{VI}Fe_{3x}²⁺^{VI}Fe_{2-2x}³⁺)O₅(OH)₄, the following equations are obtained for $\kappa + \gamma$ mixtures and $\kappa + \phi$ mixtures, respectively:

$$\begin{bmatrix} Si \\ Al \\ Fe^{3+} \\ Fe^{2+} \end{bmatrix} = \begin{bmatrix} 1.99 & 2 & -1 \\ 1.98 & 0 & 0 \\ 0.03 & 0 & 2 \\ 0 & 3 & -1 \end{bmatrix} \times \begin{bmatrix} \kappa \\ \gamma \\ \gamma x \end{bmatrix} \quad (2)$$

$$\begin{bmatrix} Si \\ Al \\ Fe^{3+} \\ Fe^{2+} \end{bmatrix} = \begin{bmatrix} 1.99 & 2 & 0 \\ 1.98 & 0 & 0 \\ 0.03 & 2 & -2 \\ 0 & 0 & 3 \end{bmatrix} \times \begin{bmatrix} \kappa \\ \phi \\ \phi x \end{bmatrix} \quad (3)$$

Both equations involve using a non-square matrix, and they are solved using a least-square method. $\kappa + \gamma$ stable

results are obtained for four particles and $\kappa + \phi$ for three of them (Table 6). In all cases, the proportion of either greenalite or cronstedtite in mixed particles remains rather low (between 12 and 18 %) in contrast with what was observed for berthierine-kaolinite particles (Table 5). Plotting the calculated compositions in the ^{VI}Fe²⁺-^{VI}Fe³⁺-^{VI}Al ternary diagram of Fig. 15 reveals that cronstedtites fall in the classical composition range, whereas greenalites appear rich in Fe³⁺ compared to reference samples.

It must be pointed out that for the two least Fe-concentrated particles of Table 4 (particles 10 and 6), no composition could be obtained as residual errors derived from the least-square analysis were too high.

Finally, for one particle only (particle 19, Table 4), a significant result could be obtained only by assuming a ternary mixture formed with 68 % kaolinite, 21 % berthierine and 11 % greenalite. In this calculation, the compositions of berthierine and greenalite were assumed to be the mean ones obtained in Tables 5 and 6. The presence of such a ternary mixture could be explained either by (1) the crystallization of different Fe-serpentine species on each basal face of initial kaolinite particle or (2) by a superimposition of two different mixed particles.

Conclusion

The detailed spectroscopic analysis presented in this study confirms the assumptions derived from our previous global investigation (Rivard et al. 2013). Indeed, whatever the investigation scale, particles obtained after reacting kaolinite with metallic iron at 90 °C in anoxic conditions appear to be intimate mixtures of kaolinite and Fe-serpentine layers. As no pure Fe-serpentine or kaolinite particles were ever observed, the mechanism in which Fe-serpentine precipitates onto kaolinite surfaces appears very likely. Furthermore, this study confirms the relevance of acquiring X-ray absorption spectroscopic data at various

edges and at different spatial resolutions as it provides strong crystal chemistry constraints for determining the nature of newly formed species.

The data obtained also reveal some variability in the nature of the newly formed Fe-rich serpentines. As a consequence, analyses down to the particle scale are required to derive meaningful unit cell formulae that strongly evolve from one particle to another. In all cases, the structure and composition of the neo-formed products place them in the berthierine–greenalite–cronstedtite domain. On the basis of XRD and Mössbauer spectroscopy (Rivard et al. 2013), these two latter minerals should be minor phases compared to berthierine, but their presence has to be considered for a complete understanding of the system. At the present time, we can propose a scenario in which precipitation of cronstedtite and greenalite phases occurs prior to berthierine formation. Indeed, we showed that kaolinite dissolution occurs in two steps with a first short period characterized by preferential Si dissolution (Rivard et al. 2013). As oxidation of metallic iron is a fast reaction, association between released Si, Fe²⁺ and Fe³⁺ should result in this first step in formation of cronstedtite and greenalite. In a second step, the congruent dissolution of kaolinite releases both Al and Si, which should favor the precipitation of berthierine. Apparently, in view of the scarcity of particles containing different Fe-serpentines, berthierine growth onto greenalite–cronstedtite surfaces appears unlikely.

In our experimental conditions, the proportion of formed berthierine is estimated to reach 10–20 % of the initial amount of clay, and this proportion is associated with a consumption of metallic iron around 93 % (Rivard et al. 2013). In spite of this high reactivity, the consequences on the properties of host clay formation in the context of radioactive waste disposal should be limited as the newly formed phase belongs to the same clay family and has consequently similar physico-chemical properties. Partial spectroscopic analyses, conducted on 1 and 3 months samples, do not evidence significant difference in comparison with 9 months sample, as it might be expected in view of chemical and mineralogical results (most of the transformations occurred during the first month). Nevertheless, to better understand the different reaction phases in the system, it would be informative to apply this combination of spectroscopic and microscopic analyses to samples with shorter reaction times, from several hours to a day or a week. These supplementary results could then provide robust equilibrium data for thermodynamic models aiming at predicting the fate of radionuclides in deep underground disposal for high activity nuclear waste.

Acknowledgments This work was financially supported by Andra (Agence nationale pour la gestion des déchets radioactifs—French

national radioactive waste management agency). The STXM data were collected at the Canadian Light Source, which is supported by the Natural Sciences and Engineering Research Council of Canada, the National Research Council Canada, the Canadian Institutes of Health Research, the Province of Saskatchewan, Western Economic Diversification Canada, and the University of Saskatchewan. We also thank SOLEIL facility for financial and technical supports. This work could not have been done without the collaboration of LUCIA beamline staff Nicolas Tercera, Anne-Marie Flank and Pierre Lagarde. We also thank Valérie Briois from SAMBA beamline for collecting data at Fe K-edge on her “home beamtime”. We gratefully thank Jaafar Ghanbaja for TEM investigations. A special thanks goes to Yves Moëlo who provided berthierine sample and to Markus Plaschke who kindly shared Fe–L edges data on reference samples so that we could operate validation tests on the fitting procedure of Fe–L spectra.

References

- Aja SU, Darby Dyar M (2002) The stability of Fe-Mg chlorites in hydrothermal solutions—I. Results of experimental investigations. *Appl Geochem* 17:1219–1239
- Bailey SW (1988) Odinite, a new dioctahedral-trioctahedral Fe³⁺-rich 1:1 clay mineral. *Clay Miner* 23:237–247
- Bardot F, Villiéras F, Michot LJ, François M, Gérard G, Cases JM (1998) High resolution gas adsorption study on illites permuted with various cations: assessment of surface energetic properties. *J Dispers Sci Technol* 19:739–759
- Belin S, Briois V, Traverse A, Idir M, Moreno T, Ribbens M (2005) SAMBA a new beamline for X-ray absorption Spectroscopy in the 4–40 keV range. *Phys Scripta* T115:980–983
- Brindley GW (1982) Chemical compositions of berthierines—a review. *Clays Clay Miner* 30:153–155
- Briois V, Vantelon D, Villain F, Couzinet B, Flank AM, Lagarde P (2007) Combining two structural techniques on the micrometer scale: micro-XAS and micro-Raman spectroscopy. *J Synchrotron Radiat* 14:403–408
- Calvert CC, Brown A, Brydson R (2005) Determination of the local chemistry of iron in inorganic and organic materials. *J Electron Spectroscop Relat Phenom* 143:173–187
- Crocobette JP, Pollak M, Jollet F, Thromat N, Gautier-Soyer M (1995) X-Ray absorption spectroscopy at the Fe L_{2,3} threshold in iron oxides. *Phys Rev B: Condens Matter* 52:3143–3150
- de Combarieu G, Barpoux P, Minet Y (2007) Iron corrosion in Callovo-Oxfordian argillite: from experiments to thermodynamic/kinetic modelling. *Phys Chem Earth* 32:346–358
- Devaraju TC, Laajoki K, Subbarao G (2000) Retrograde chlorite-bearing greenalite from the iron-formation of Kudremukh, Karnataka, India. *Neues Jahrbuch für Mineralogie, Monatshefte* 5:207–216
- Farges F, Lefrère Y, Rossano S, Berthereau A, Calas G, Brown GE Jr (2004) The effect of redox state on the local structural environment of iron in silicate glasses: a combined XAFS spectroscopy, molecular dynamics, and bond valence study. *J Non-Cryst Solids* 334:176–188
- Flank AM, Cauchon G, Lagard P, Bac S, Janousch M, Wetter R, Dubuisson JM, Idir M, Langlois F, Moreno T, Vantelon D (2006) LUCIA, a microfocus soft XAS beamline. *Nucl Instrum Methods Phys Res, Sect A* 246:269–274
- Geiger CA, Henry DL, Bailey SW, Maj JJ (1983) Crystal structure of cronstedtite-2H₂. *Clays Clay Miner* 31:97–108
- Guggenheim S, Bailey SW (1989) An occurrence of a modulated serpentine related to the greenalite-caryopilite series. *Am Miner* 74:637–641

- Hitchcock AP (2001) Soft X-ray spectromicroscopy of polymers and biopolymer interfaces. *J Synchrotron Radiat* 8:66–71
- Ildefonse Ph, Cabaret D, Sainctavit Ph, Calas G, Flank AM, Lagarde P (1998) Aluminium X-ray absorption near edge structure in model compounds and Earth's surface minerals. *Phys Chem Miner* 25:112–121
- Jacobsen C, Wirick S, Flynn G, Zimba C (2000) Soft X-Ray spectroscopy from image sequences with sub-100 nm spatial resolution. *J Microsc* 197:173–184
- Kaznatcheev KV, Karunakaran Ch, Lanke UD, Urquhart SG, Obst M, Hitchcock AP (2007) Soft X-ray spectromicroscopy beamline at the CLS: commissioning results. *Nucl Instrum Methods Phys Res, Sect A* 582:96–99
- Kogure T (2002) Identification of polytypic groups in hydrous phyllosilicates using electron back-scattering patterns. *Am Miner* 87:1678–1685
- Kohler E (2001) Réactivité des mélanges synthétiques smectite/kaolinite et smectite/aluminium gel en présence d'un excès de fer métal. Dissertation (DRRT) Evry Val d'Essonne University
- Lerotic M, Jacobsen C, Schäfer T, Vogt S (2004) Cluster analysis of soft X-ray spectromicroscopy data. *Ultramicroscopy* 100:35–57
- Lerotic M, Jacobsen C, Gillow JB, Francis AJ, Wirick S, Vogt S, Maser J (2005) Cluster analysis in soft X-ray spectromicroscopy: finding the patterns in complex specimens. *J Electron Spectrosc Relat Phenom* 144–147:1137–1143
- Li D, Bancroft GM, Fleet ME, Feng XH (1995a) Silicon K-edge XANES spectra of silicate minerals. *Phys Chem Miner* 22:115–122
- Li D, Bancroft GM, Fleet ME, Feng XH, Pan Y (1995b) Al K-edge XANES spectra of aluminosilicate minerals. *Am Miner* 80:432–440
- Mermut AR, Cano AF (2001) Baseline studies of the clay mineral society source clays: chemical analyses of major elements. *Clays Clay Miner* 49:381–386
- Miot J, Benzerara K, Morin G, Kappler A, Bernard S, Obst M, Férard C, Skouri-Panet F, Guigner JM, Posth N, Galvez M, Brown GE Jr, Guyot F (2009) Iron biomineralization by anaerobic neutrophilic iron-oxidizing bacteria. *Geochim Cosmochim Acta* 73:696–711
- Newville M (2001) EXAFS analysis using FEFF and FEFFIT. *J Synchrotron Radiat* 8:96–100
- Newville M, Livin P, Yacoby Y, Rehr JJ, Stern EA (1993) Near-edge x-ray-absorption fine structure of Pb: a comparison of theory and experiment. *Phys Rev B: Condens Matter* 47:14126–14131
- Perronnet M (2004) Réactivité des matériaux argileux dans un contexte de corrosion métal. Application au stockage des déchets radioactifs en site argileux. PhD Thesis INPL Nancy
- Ravel B, Newville M (2005) ATHENA, ARTEMIS, HEPHAESTUS: data analysis for X-ray absorption spectroscopy using IFEFFIT. *J Synchrotron Radiat* 12:537–541
- Rivard C, Pelletier M, Michau N, Razafitianamaharavo A, Bihannic I, Abdelmoula M, Ghanbaja J, Villiéras F (2013) Berthierine-like mineral formation and stability during the interaction of kaolinite with metallic iron at 90°C under anoxic and oxidant conditions. *Am Miner* 98: xxx–xxx (In Press)
- Schlegel ML, Bataillon C, Benhamida K, Blanc C, Menut D, Lacour JL (2008) Metal corrosion and argillite transformation at the water-saturated, high-temperature iron-clay interface: a microscopic-scale study. *Appl Geochem* 23:2619–3263
- Shaw SA, Peak D, Hendry J (2009) Investigation of acidic dissolution of mixed clays between pH 1.0 and –3.0 using Si and Al X-ray absorption near edge structure. *Geochim Cosmochim Acta* 73:4151–4165
- Teo BK (1986) EXAFS: basic principles and data analysis. *Inorganic chemistry concepts*, vol 9. Springer, Berlin
- Van Aken PA, Liebscher B (2002) Quantification of ferrous/ferric ratios in minerals: new evaluation schemes of Fe-L_{2,3} electron energy-loss near-edge spectra. *Phys Chem Miner* 29:188–200
- Van der Laan G, Kirkman IW (1992) 2p absorption spectra of 3d transition metal compounds in tetrahedral and octahedral symmetry. *J Phys: Condens Matter* 4:4189–4204
- Vantelon D, Montarges-Pelletier E, Michot LJ, Brioso V, Pelletier M, Thomas F (2003) Iron distribution in the octahedral sheet of dioctahedral smectites. An Fe K-edge X-ray absorption spectroscopy study. *Phys Chem Miner* 30:44–53
- Wasinger E, de Groot FMF, Hedman B, Hodgson KO, Solomon EI (2003) L-edge X-ray absorption spectroscopy of Non-Heme Iron sites: experimental determination of differential orbital covalency. *J Am Chem Soc* 125:12894–12906
- Wilke M, Farges F, Petit PE, Brown GE Jr, Martin F (2001) Oxidation state and coordination of Fe in minerals: an Fe K-Xanes spectroscopic study. *Am Miner* 86:714–730
- WWW-MINCRYST (2012) Crystallographic and crystallochemical database for minerals and their structural analogues. <http://database.iem.ac.ru/mincryst>